RESEARCH

Modelling fracture due to corrosion and mechanical loading in reinforced concrete

J. Alfaiate · L. J. Sluys · A. Costa

Abstract Corrosion in reinforced concrete is an important feature which can lead to increased deformation and cracking, as well as to premature failure. In the present work, macro-mechanical modelling of corrosion is performed, namely the degradation of bond–slip between concrete and steel. A mixed-mode damage model is adopted, in which the interaction between the bond–slip law and the stress acting in the neighbourhood of the concrete–steel bar interface is taken into account. Bond–slip degradation is modelled using an evolutionary bond–slip relationship, which depends on the level of corrosion. Different relevant loading cases are studied. Special attention is given to the evolution of corrosion in time, under constant load. This is done by adopting a Total Iterative Approach, in which the structure is reevaluated each time step, upon damage increase due to corrosion. Pullout tests are presented to illustrate the performance of the model. Bending tests are also performed to evaluate the influence of corrosion at structural level.

Keywords Corrosion · Reinforced concrete · Total Iterative Approach

J. Alfaiate (✉) · A. Costa
Department of Civil Engineering, CERIS, Instituto Superior Técnico, Universidade de Lisboa, Av. Rovisco Pais, 1, 1049-001 Lisbon, Portugal
e-mail: jorge.alfaiate@tecnico.ulisboa.pt

A. Costa
e-mail: antonio.silva.costa@tecnico.ulisboa.pt

L. J. Sluys
Department of Civil Engineering and Geosciences, Delft University of Technology, P.O. Box 5048, 2600 GA Delft, The Netherlands
e-mail: L.J.Sluijs@tudelft.nl

List of symbols

DSDA	Discrete strong discontinuity approach
IA	Incremental approach
TIA	Total Iterative Approach
$\lvert \cdot \rvert$	The norm of (.)
C	Control loading function used with the Total Iterative Approach
c_0	Initial cohesion
c	Cohesion
d	Scalar damage variable
$\mathbf{d}$	Second order damage tensor
d_n	Normal damage variable component
d_s	Shear damage variable component
D_{nn}	Normal diagonal component of tensor $\mathbf{D}_{\Gamma_d}^{el}$
D_{ss}	Shear diagonal component of tensor $\mathbf{D}_{\Gamma_d}^{el}$
$\mathbf{D}_{\Gamma_d}^{el}$	Second order elastic constitutive tensor
Δ	Increment
f_1, f_2	Limit surfaces defined in the traction space
f_{t0}	Initial tensile strength
f_t	Tensile strength
$\mathbf{F}$	Applied force vector
G_F	Fracture energy
G_F^{II}	Fracture energy under mode-II fracture

Springer

g_n	Normal damage evolution law
g_s	Shear damage evolution law
κ	Monotonic increasing function of the displacement jump components
λ	Loading factor
ρ	κ_s/κ_n
$\boldsymbol{\sigma}$	Stress tensor
$\boldsymbol{\varepsilon}$	Strain tensor
$\mathbf{t}$	Traction vector acting at the discontinuity
t_n	Normal component of the traction vector
t_s	Shear component of the traction vector
$\mathbf{w}$	Displacement jump vector
w_n	Normal component of the jump displacement vector
w_s	Shear component of the jump displacement vector
ϕ	Internal friction angle; diameter of reinforcement bar

1 Introduction

Corrosion of steel in reinforced concrete structures is one of the main causes of structural deterioration. It has a major influence on the service life of the structure as well as in the Serviceability Limit State, giving rise to the increase of both deformation and cracking.

The mechanism of steel corrosion is complex, based on chemo-hygro-thermo-mechanical processes (Ožbolt et al. 2017). In this work, only macroscale modelling of the mechanical behaviour is addressed.

Reinforced concrete exhibits nonlinear behaviour, namely due to:

(i) cracking,
(ii) hardening compressive behaviour,
(iii) crushing,
(iv) nonlinear-plastic behaviour of reinforcement steel,
(v) bond–slip between concrete and steel.

Steel corrosion gives rise to three main mechanical effects which further contribute to nonlinear behaviour:

(vi) degradation of the bond–slip relationship between concrete and steel,
(vii) reduction of the resistant cross section area of the steel bars, also designated by core reduction hereafter,

(viii) expansion of the steel cross section due to the formation of rust around the steel bars, which may cause delamination and spalling of the cover.

On the other hand, there are many factors that can influence corrosion by affecting the bond–slip relationship, namely related to the concrete composition and the stress state (see for instance Louro 2014; Bastos 2022). A non exhaustive list of some important factors is given:

1. environment, which affects both the level and the rate of corrosion,
2. concrete compressive strength,
3. degree of confinement in the neighbourhood of the reinforcement steel due to stirrups,
4. stress state in the neighbourhood of the concrete–steel interface, which can lead to an increase of the bond strength under compression, or to a decrease of the bond strength under tension,
5. the bond index: ratio of bearing area[1] to the shearing area,[2]
6. the packing density: the ratio of the volume of solids to the sum of the volume of solids and voids,
7. the bar diameter, which can give rise to a decrease of the bond strength with the increase of the diameter,
8. the recycled agreggate content or other aspects of the concrete constitution, as in the case of low binder concrete or low cement recycled aggregate concrete, for example,...

There has been considerable research on the degradation of bond strength due to steel corrosion. For instance, the relation between surface crack width and steel to concrete bond has been experimentally investigated, under artificially induced corrosion (Apostolopoulos et al. 2022; Mak et al. 2019) and natural induced corrosion over time (Tahershamsi et al. 2016). From these studies, analytical models have been proposed.

Spalling is also an important issue, which depends heavily on the level of confinement, induced by stirrups (3) or compressive stress state (2). Recent experimental research work has been published considering the effects of stirrup confinement and concrete cover on the bond strength (Lin and Zhao 2016; Mak and Lees 2022), as well as stirrup corrosion (Zhou et al. 2017).

---

[1] Projected rib area normal to the bar axis.

[2] Bar perimeter times centre-to-centre distance between ribs.

Important numerical work can also be found in the literature, namely regarding the evolution of radial cracking due to the expansion of corroded products (Guzmán et al. 2011, 2014; Guzmán and Gálvez 2017; Sanz et al. 2016).

However, reliable predictions of bond strength degradation or decrease of the structural strength due to corrosion are still lacking (Koulouris and Apostolopoulos 2021). A numerical approach is presented here, with a twofold purpose—(i) the modelling of bond degradation at local level and (ii) the evaluation of premature structural failure. In the structural tests, the solutions with corrosion are compared to the non-corroded solution, which is taken as reference.

In this work, the main focus is on: (vi) the deterioration of the bond–slip relationship, as well as on (vii) the reduction of the sane cross section of the reinforcement bars. Factors (1), (2) and (4) are also covered. Moreover, all nonlinear aspects of concrete behaviour (i) to (v) are taken into account. In future works, the main focus will be on spalling of the concrete cover (viii), as well as on the dependence of corrosion on stirrup confinement (3). Additionally, upon completion of the full mixed-mode formulation involved in the analysis of spalling, comparison to experimental tests will also be addressed.

In Sect. 2 a description of the corrosion effects is given. The mechanical model is described in Sect. 2.2, which is divided into: (i) the mixed-mode fracture model, (ii) the evaluation of the reduced area of the sane cross section as well as the percentage of rust and (iii) the degradation of the bond–slip relationship. The latter is modelled adopting different transition modes between pre-corrosion and final corrosion stage, which consists of a novel aspect of this work. Special attention is given to the the *passive* evolution of corrosion, which affects the structure in time. In this case, degradation occurs under stabilised loading, with corresponding stiffness decrease. The increase of corrosion leads to an increase of damage at the bond–slip level. Keeping the external loading fixed, it is not straightforward to take this effect into account with an incremental approach. This is why a Total Iterative Approach (TIA) is adopted in the present work (Alfaiate and Sluys 2023), in which a new control function is introduced such that damage is driven by the increase of corrosion. The use of the TIA to model corrosion is another novel aspect of this work. The Total Iterative Approach adapted to the study of corrosion is described in Sect. 3, after a brief review

of the conventional Total Approach. In Sect. 4, some pullout tests and bending tests are presented with different approaches to corrosion. In particular, the following aspects are evaluated: (i) degradation of the bond–slip law due to corrosion, (ii) reduction of the reinforcement bar effective cross section, (iii) dependence of the bond–slip law on the the stress normal to the interface, (iv) rate of corrosion and (v) slippage of the reinforcement bar at the anchorage zone. Finally, in Sect. 5 some conclusions are drawn.

2 Corrosion

2.1 Empirical model

Many empirical models, based on experimental evidence, have been used to predict the evolution of corrosion in reinforcement steel (see for instance Chernin and Val 2011). In the present work, the corrosion model proposed by Fang et al. (2004) is adopted, in which uniform corrosion around the bar is assumed.

The corrosion level η is defined by (see Fig. 1):

$$\eta = \frac{A_0 - A}{A_0}, \tag{1}$$

where A_0 is the initial cross section area of the bar and A is the uncorroded cross section area of the bar, after removing the corrosion sub-products. The corrosion level evolves from 0 to η_f, the latter corresponding to the final corrosion stage.

In Fig. 1, r_0 is the radius of the initial cross section area $(A_0 = \pi r_0^2)$, x is the penetration of the corrosion giving rise to a reduction of the sane cross section of the bar and a is the increase of the radius due to the formation of rust. In order to take into account the length of the corroded zone, one other parameter v is defined
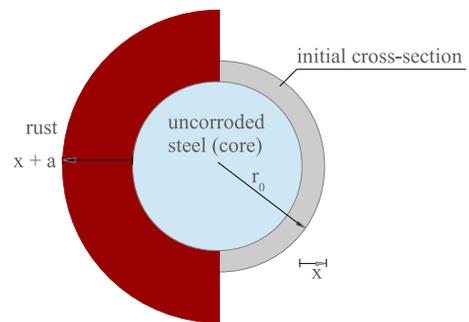

Fig. 1 Corrosion: uncorroded steel and formation of rust

as the volume increase due to the formation of rust, with respect to the volume of uncorroded steel. Corrosion of the steel bars can occur in a restricted length, as in chloride induced corrosion, or along a considerable length of the bars, usually due to carbonation induced corrosion. In the former case, a reduction of the strength is obtained locally, due to the decrease of the cross section of the steel bar. In the latter case, a significant loss of adherence between concrete and steel can occur. Thus, the increase of the corroded volume is variable and depends on the type of product inflicting corrosion. A value $v = 2$ was adopted in Andrade et al. (1993), Molina et al. (1993), Coronelli (1998) and Lundgren (2005) and is considered a reference value.

According to Fang et al. (2004), Silva (2018), the increase of the radius due to the formation of rust can be evaluated as:

$$a = -r_0 + \sqrt{r_0^2 + (v - 1) \times (2r_0 x - x^2)}, \qquad (2)$$

where $v = 2$. Since

$$\eta = \frac{A_0 - A}{A_0} = \frac{r_0^2 - (r_0 - x)^2}{r_0^2}, \qquad (3)$$

or

$$\eta r_0^2 = 2r_0 x - x^2, \qquad (4)$$

we obtain,

$$a = -r_0 + \sqrt{r_0^2 + \eta r_0^2}. \qquad (5)$$

Defining

$$r_f = r_0 + a = r_0 \sqrt{1 + \eta}, \qquad (6)$$

the expansion of the cross section of the bar due to corrosion gives rise to the strain value:

$$\varepsilon^{corr} = \frac{r_f - r_0}{r_0} = \sqrt{1 + \eta} - 1. \qquad (7)$$

2.2 Mechanical model

In this Section a mixed-mode bond–slip model is reviewed. Corrosion of the reinforcement steel gives rise to three main mechanical aspects: (i) reduction of the resistant cross section area of the steel bar, (ii) expansion of the steel cross section due to the formation of rust around the steel bar and (iii) degradation of the bond–slip relationship between concrete and steel. These aspects are also discussed in the following.

2.2.1 Mixed-mode bond–slip model

The bond–slip relationship between concrete and steel is modelled using a mixed-mode damage model (Alfaiate and Sluys 2017a). This model was developed within the scope of a discrete crack (or strong discontinuity) approach, defining the relationship between discontinuity displacement jumps and tractions. The damage evolution law is driven by the traction field and the limit surface in the traction space shown in Fig. 2 is defined. As a consequence, this model allows for the interaction between: (i) the bond traction and (ii) the bulk stress normal to the concrete–steel interface as well as the normal traction at the interface, such that compressive confinement as well as spalling can be taken into account. For more detailed information on the mixed-mode fracture model the reader may also be referred to the works presented in Alfaiate and Sluys (2017a, b, 2019).

In this work, the following relationship is adopted:

$$\begin{aligned} t_n &= (1 - d_n)D_{nn}w_n \\ t_s &= (1 - d_s)D_{ss}w_s, \end{aligned} \qquad (8)$$

where t_n is the traction normal to the discontinuity, t_s is the traction tangent to the discontinuity, here defined as the bond stress, w_n is the normal jump displacement, w_s is the sliding jump displacement or slip displacement, d_n is the damage under normal traction, d_s is the damage variable under bond–slip and D_{nn}, D_{ss} are the normal and shear elastic stiffness coefficients, respectively, corresponding to the diagonal components of the elastic constitutive tensor at discontinuity Γ_d, $\mathbf{D}_{\Gamma_d}^{el}$.

The limit surface (Fig. 2) is dependent on material strength parameters, namely:

$$f_t = f_t(g_n(\kappa_n)) = g_n(\kappa_n)D_{nn}\kappa_n, \qquad (9)$$

$$c = c(g_s(\kappa_s)) = g_s(\kappa_s)D_{ss}\kappa_s, \qquad (10)$$

where f_t is the tensile strength, which is dependent on a scalar variable κ_n, c is the cohesion, which is dependent on a scalar variable κ_s and g_n and g_s are damage evolution laws under mode-I and mode-II, respectively:

$$\begin{aligned} g_n(\kappa_n) &= 1 - d_n \\ &= \frac{f_t}{D_{nn}\kappa_n}, \quad \text{under mode-I fracture,} \end{aligned} \qquad (11)$$

$$\begin{aligned} g_s(\kappa_s) &= 1 - d_s \\ &= \frac{c}{D_{ss}\kappa_s}, \quad \text{under mode-II fracture.} \end{aligned} \qquad (12)$$

Fig. 2 Limit surface in the traction space
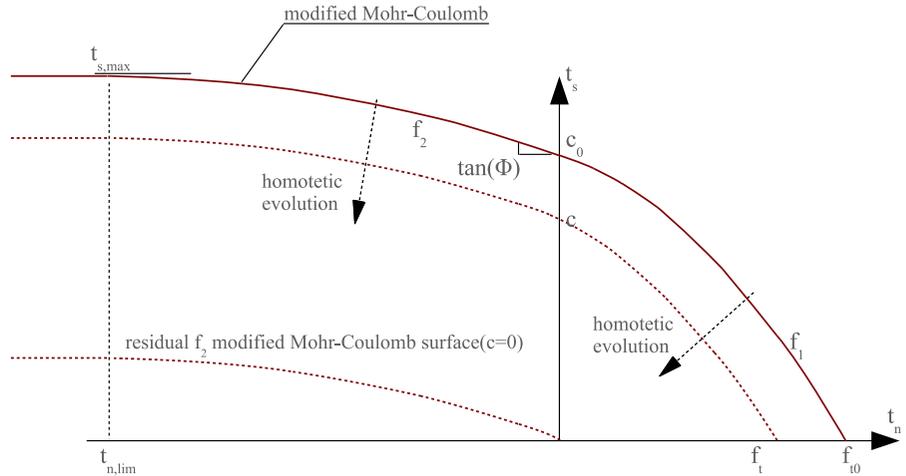
Assuming exponential softening, Eqs. (11) and (12) become:

$$g_n = 1 - d_n = \frac{\kappa_{n0}}{\kappa_n} \exp\left[\frac{-f_{t0}}{G_F}(\kappa_n - \kappa_{n0}) \right], \qquad (13)$$

$$g_s = 1 - d_s = \frac{\kappa_{s0}}{\kappa_s} \exp\left[\frac{-c_0}{G_F^{II}}(\kappa_s - \kappa_{s0}) \right], \qquad (14)$$

where G_F and G_F^{II} are the fracture energy and the fracture energy under mode-II fracture, respectively. The scalar variables κ_n and κ_s are defined such that: $\kappa_n = w_n$ under pure mode-I fracture and $\kappa_s = |w_s|$ under pure mode-II fracture. In Eqs. (13) and (14), $\kappa_{n0} = f_{t0}/D_{nn}$ and $\kappa_{s0} = c_0/D_{ss}$, where f_{t0} and c_0 are the initial tensile strength and initial cohesion, respectively (see Fig. 2). For mode-I fracture and mode-II fracture we obtain, respectively,

$$f_t = f_{t0} \exp\left[\frac{-f_{t0}}{G_F}(\kappa_n - \kappa_{n0}) \right], \qquad (15)$$

$$c = c_0 \exp\left[\frac{-c_0}{G_F^{II}}(\kappa_s - \kappa_{s0}) \right]. \qquad (16)$$

Mixed-mode fracture is defined under $w_n > 0$, whereas mode-II fracture due to compressive states is defined under $w_n = 0 \wedge t_n < 0$. The limit surface in the traction space is defined by two functions: f_1 and f_2, in which f_1 is valid for $t_n \geq 0$ and f_2 is valid under compressive tractions ($t_n < 0$), respectively (see Fig. 2). Function f_1 is given by:

$$f_1 = 0 \Leftrightarrow |t_s| = \frac{f_t \tan(\phi) - c}{f_t^2} t_n^2$$
$$- \tan(\phi) t_n + c, \quad (t_n > 0). \qquad (17)$$

For f_2 function a modified Mohr–Coulomb surface is adopted:

$$f_2 = 0$$
$$\Leftrightarrow \begin{cases} |t_s| = \frac{\tan(\phi)}{2 t_{n,lim}} t_n^2 - \tan(\phi) t_n + c, & \text{if } t_{n,lim} \leq t_n \leq 0 \quad \text{(i)} \\ |t_s| = t_s(t_{n,lim}) = t_{s,max}, & \text{if } t_n < t_{n,lim} \quad \text{(ii)}, \end{cases}$$
$$(18)$$

In Eqs. (17) to (18), ϕ is the internal friction angle of the discontinuity and in (18) $t_{n,lim}$ is the normal traction corresponding to the maximum shear traction (such that $\partial f_2/\partial t_n = 0$, see Fig. 2). From (17) and (18), is is clear that the transition between functions f_1 and f_2 is continuous, with continuous derivative:

$$\frac{\partial f_1}{\partial t_n}_{|t_n=0} = \frac{\partial f_2}{\partial t_n}_{|t_n=0} = \tan(\phi). \qquad (19)$$

Damage initiation is defined according to:

$$f_1(f_{t0}, c_0) = 0 \quad \vee \quad f_2(c_0, t_{n,lim}) = 0, \qquad (20)$$

where dependence on $t_{n,lim}$ is only relevant for surface f_2.

In the present study, isotropic damage evolution is adopted whenever the normal traction is positive; otherwise, a dummy stiffness is adopted for the normal coefficient D_{nn}:

$$d_n = d_s \quad \text{if } t_n > 0 \quad \text{(i.)}$$
$$d_n = 0 \wedge D_{nn} \approx \infty \quad \text{if } t_n \leq 0 \quad \text{(ii.)}. \qquad (21)$$

In this way, the loss of normal stiffness is modelled in (i.) due to the bond degradation between concrete and steel, enabling the formation of cracking parallel to the steel bar. Since damage can only increase, different damage variables d_n^+ and d_n^- must be defined, under

tensile normal traction and under compressive normal traction, respectively (Alfaiate and Sluys 2017a, b, 2019).

In all cases, although both internal variables κ_n, κ_s remain functions of $\mathbf{w}$: $\kappa_n = \kappa_n(\mathbf{w})$, $\kappa_s = \kappa_s(\mathbf{w})$, they do not vary if the traction state remains on the limit surface $f_1 \vee f_2$:

$$\dot{f}_1 = 0 \Rightarrow (\dot{\kappa}_n = 0 \wedge \dot{\kappa}_s = 0),$$
$$\dot{f}_2 = 0 \Rightarrow \dot{\kappa}_s = 0. \qquad (22)$$

Furthermore, if variables κ_n and κ_s increase, the stress state must remain on the surface:

$$\dot{\kappa}_n > 0 \Rightarrow \dot{f}_1 = 0,$$
$$\dot{\kappa}_s > 0 \Rightarrow (\dot{f}_1 = 0 \wedge \dot{f}_2 = 0). \qquad (23)$$

As a consequence, both the Kuhn–Tucker conditions and the consistency condition are satisfied:

$$\dot{d}_n \geq 0, \quad \dot{d}_s \geq 0, \quad f \leq 0,$$
$$\dot{d}_n f = 0, \quad \dot{d}_s f = 0, \quad \dot{d}\dot{f} = 0. \qquad (24)$$

2.2.2 Cross section

Given the level of corrosion (1), it is possible to obtain both the core reduction x and the expansion value a. From (4) we obtain

$$x = r_0 \left(1 - \sqrt{1 - \eta} \right), \qquad (25)$$

or

$$r_{sane} = r_0 - x = r_0 \sqrt{1 - \eta}, \qquad (26)$$

whereas the expansion value a is obtained from (5):

$$a = -r_0 \left(1 - \sqrt{1 + \eta} \right), \qquad (27)$$

giving rise to,

$$r_f = r_0 + a = r_0 \sqrt{1 + \eta}. \qquad (28)$$

2.2.3 Bond–slip degradation

The main issue regarding bond–slip degradation is how to perform the transition between the original pre-corrosion law and the bond–slip law, corresponding to the final corrosion stage η_f. For each level of corrosion η, an intermediate bond–slip law is defined, with corresponding increase of damage. According to the Kuhn–Tucker conditions (24), any material point, defined by the jump displacement and the traction state $(\mathbf{w} - \mathbf{t})$, should lie on the current, intermediate law. In Fig. 3,

the uniaxial representation of the transition between the previous bond–slip law η_{t-1} and the actual one η_t, is illustrated. In this Figure, the bond–slip laws corresponding to both the pre-corrosion level ($\eta = 0$) and to the final corrosion level $\eta = \eta_f$ are also depicted. For a multilinear relationship, each point $m : w_s(m), t_s(m)$ on the current law is obtained, keeping abcissa $w_s(m)$ fixed, by

$$t_s(m) = t_{s0}(m) + [t_{sf}(m) - t_{s0}(m)] \times \frac{\eta_t}{\eta_f} \qquad (29)$$

In (29), t_s is the bond stress lying on the limit surface, corresponding to the actual law ($\eta = \eta_t$), t_{s0} is the bond stress corresponding to the initial pre-corrosion law ($\eta = 0$) and t_{sf} is the bond stress corresponding to the final corrosion stage ($\eta = \eta_f$). Four different transition modes from the previous state η_{t-1} to the current state η_t are represented:

1. from $a \rightarrow b$, the increase in the slip displacement w_s leads to an increase of the bond stress t_s;
2. from $a \rightarrow c$ the bond stress is kept constant;
3. from $d \rightarrow e$ the slip displacement is kept constant and the bond stress drops;
4. from $a \rightarrow f$ the bond stress is kept constant and only slipping takes place.

Case 1, also designated hereafter as *variable loading*, is only admissible if both loading and corrosion increase simultaneously. However, if corrosion is increasing under constant loading, the slip value w_s^b, corresponding to position b, can not be reached. Instead, the material point should lie on the current law such that the bond stress t_s remains constant, limiting the value of the slip displacement to w_s^c (case 2, also designated hereafter as *fixed loading*. Similarly, if the slip displacement is kept fixed instead of the bond stress, a drop in the bond stress occurs ($d \rightarrow e$, case 3). Note that, cases 1 and 2 are only possible whenever the bond stress is smaller than the current (intermediate) cohesion, $|t_s| < c_t$. Otherwise, either (i) failure would occur—under stress control—or (ii) the load would drop and the material point would lie on the softening part of the current bond–slip law—under displacement control.

In case 2, a limitation on the slip displacement value w_s^c is introduced. This limit value depends on the actual bond–slip law, which depends on the corrosion rate. As a consequence, if the *true* corrosion rate is implemented, a severe limitation is imposed numerically on the time step such that, for each corrosion stage η_t, this

Fig. 3 Transition between bond–slip laws with increasing corrosion: $a \rightarrow b$ increase of both load and corrosion, $a \rightarrow c$ and $a \rightarrow f$ increasing corrosion under constant load, $d \rightarrow e$ increasing corrosion under constant slip displacement
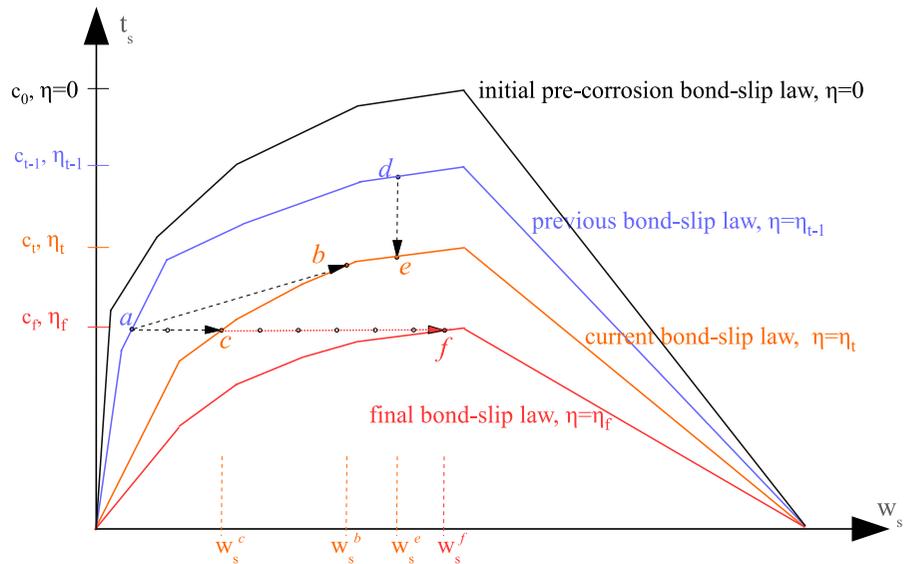
w_s^c value can not be overcome. Here, a simplified procedure is introduced, by defining the ultimate slip displacement on the final bond–slip law, w_s^f, corresponding to case 4. Thus, under constant load, the material point should lie on the *plateau* defined from $a \rightarrow f$, independently from the rate of corrosion. This procedure allows for a more flexible definition of the time step factor, which is an important feature of the Total Iterative Approach, as described in Sect. 3.2. Moreover, a smooth transition is allowed under displacement control from the pre-softening stage to softening behaviour, as discussed above.

3 Numerical implementation

3.1 The total approach

The Total Approach was inspired by the Sequential Linear Approach (DeJong et al. 2008; Rots 2001; Rots and Invernizzi 2003; Rots et al. 2008; Slobbe et al. 2012) as well as the Lattice Models, (Lilliu and van Mier 2003; Schlangen and van Mier 1992). Departing form an equilibrium state, damage is forced to increase at material points, according to a pre-defined scheme. First, a *trial* step is adopted such that the limit surface is reached at one material point, closest to the surface, designated the critical point. Next, the *true* step is performed and damage is increased at this critical material point.

In the conventional Total Approach, as well as in all methods presented in Alfaiate and Sluys (2018), Chenjie (2019), Costa et al. (2012, 2013), Gago et al. (2011), Costa and Alfaiate (2006), the approximation of the internal variables is not exact, leading to a mismatch regarding the evaluation of the secant stiffness. This mismatch is due to the fact that, in all these methods, only one critical material point is considered for damage update.

3.2 The total iterative approach

In the present work, a Total Iterative Approach is adopted in which damage is updated, iteratively, on several material points simultaneously (Alfaiate and Sluys 2023).

Consider the case of non-proportional loading, in which the current external force vector $\mathbf{F}_2$ is applied on top of the previous ones, accumulated in $\mathbf{F}_1$, giving rise to the corresponding stresses and tractions, $\boldsymbol{\sigma}_1, \boldsymbol{\sigma}_2$ and $\mathbf{t}_1, \mathbf{t}_2$, respectively. Assume that a certain load level was reached in step $i - 1$: $\mathbf{F}_1 + \lambda_{i-1}\mathbf{F}_2$, where λ_{i-1} is the step factor adopted in step $i - 1$. In the current step i, the same load level is applied, which should lead to local solutions not lying on the surface ($f \neq 0$). For instance, departing from the limit surface given in (17) and assuming $f > 0$, we get:

$$|t_{s1} + \lambda_{i-1}t_{s2}| > \frac{f_t \tan(\phi) - c}{f_t^2}(t_{n1} + \lambda_{i-1}t_{n2})^2$$

$$-\tan(\phi)(t_{n1} + \lambda_{i-1}t_{n2}) + c. \quad (30)$$

In the conventional Total Approach (Sect. 3.1), a new loading factor λ_i in the *Trial step* is determined such that $f = 0$ at the most critical material point:

$$\left[|t_{s1} + \lambda_i t_{s2}| = \frac{f_t \tan(\phi) - c}{f_t^2}(t_{n1} + \lambda_i t_{n2})^2 \right.$$
$$\left. -\tan(\phi)(t_{n1} + \lambda_i t_{n2}) + c\right]_{crit}, \quad (31)$$

in which the internal variables as well as strength values f_t and c are kept fixed. Here, an iterative procedure is introduced such that, *for all* points lying outside the surface ($f > 0$), damage is increased until $f \approx 0$ in all these points. For all points lying outside the surface, Eq. (31) becomes:

$$|t_{s1} + \lambda_i^* t_{s2}| = \frac{f_t^* \tan(\phi) - c^*}{f_t^{*2}}(t_{n1} + \lambda_i^* t_{n2})^2$$
$$-\tan(\phi)(t_{n1} + \lambda_i^* t_{n2}) + c^*, \quad (32)$$

where f_t^* and c^* denote new tensile and cohesion strength values, respectively, corresponding to the increase of damage (see Eqs. (9) and (10)).

In the iterative procedure, step λ_i^* is no longer dependent on the condition $f = 0$ at one single critical point; instead, it will be defined in each iteration, according to a control loading function C. This function can be dependent on the displacements, forces, displacement jumps, as well as internal variables such as damage. Thus, at each step i and each iteration j, step size λ_i^j is defined such that $C = 0$, where $C = C(\mathbf{u}_1 + \lambda_i^j \mathbf{u}_2, \mathbf{F}_1 + \lambda_i^j \mathbf{F}_2, \mathbf{w}_1 + \lambda_i^j \mathbf{w}_2, \mathbf{d}_1 + \lambda_i^j \mathbf{d}_2, \ldots)$. Usually, C corresponds to a monotonic increasing function of some parameter, taken as an absolute value, similar to the constrained functions used for the arc length method.[3] For instance, in a structure exhibiting hardening behaviour, function C can be given as:

$$C = 0 \Leftrightarrow F_{k,1} + \lambda_i^j F_{k,2} - F_{i-1,k} = \Delta F_k^*, \quad (33)$$

where k is a chosen degree of freedom (dof) and ΔF_k^* is a prescribed force increment at this degree of freedom. Since $F_{i-1,k} = F_{1,k} + \lambda_{i-1}F_{k,2}$, Eq. (33) can be written as:

$$C = \lambda_i^j F_{k,2} - (\lambda_{i-1}F_{k,2} + \Delta F_k^*)$$
$$= \lambda_i^j F_{k,2} - (F_{i-1,k,2} + \Delta F_k^*), \quad (34)$$

---

[3] In fact, this function only needs to be monotonic, but if the absolute value of the control parameter is adopted then we get a monotonic increasing function in all cases.

where $i - 1$ is the previous final step. As a consequence, force F_k increases monotonically ΔF_k^* in each step. This is a particular advantage with respect to the conventional Total Approach since, in the latter, there is no control a priori of the step size.

Some examples of C functions are given below:

1. monotonic increase of force at dof k:

$$C = \lambda_i^j F_{k,2} - (\lambda_{i-1}F_{k,2} + \Delta F_k^*), \quad (35)$$

2. monotonic increase of displacement at dof k:

$$C = \lambda_i^j u_{k,2} - (\lambda_{i-1}u_{k,2} + \Delta u_k^*), \quad (36)$$

3. monotonic increase of normal or shear jump displacement w at discontinuity c:

$$C = \lambda_i^j w_{c,2} - (\lambda_{i-1}w_{c,2} + \Delta w_c^*), \quad (37)$$

4. monotonic increase of damage at material point m:

$$C = d_{i,m}^j - (d_{m,i-1} + \Delta d_m^*), \quad (38)$$

Although control function (35) is adequate for hardening behaviour only, functions (36) to (38), can also be used for softening behaviour. Function (37) is usually adopted in more critical cases, such as snap-back, in which monotonic increase of the displacement jump between faces of a discontinuity is known to occur (Alfaiate and Sluys 2023).

Reviewing the four situations presented in Sect. 2.2 corresponding to cases 1 to 4, both functions (35) and (36) could be used in case 1, whereas functions (36), (37) and (38) could be used in cases 2. and 4. In case 3, either function (36) or (37) could be adopted.

The increase of corrosion level $\Delta \eta$ can be associated to one of the variables defined in (35) to (38). For instance, if function (36) is adopted, the solution is still driven by the monotonic increase of the displacement at dof k, Δu_k^*. In this case, the rate of corrosion is given, in each step, by $\Delta \eta^*/\eta_f = \Delta u_k^*/u_{k,final}$, where $\Delta \eta^* = \eta_t - \eta_{t-1}$, η_t is the current corrosion level and $u_{k,final}$ is some predefined ultimate displacement value u_k, reached at the final corrosion stage η_f.

However, in order to better approximate a common situation in reinforced concrete structures, the solution can also be driven explicitly by the increase of corrosion. For this purpose, a new C function is defined:

$$C = \lambda_i^j - \left(\lambda_{i-1} + \frac{\Delta \eta^*}{\eta_f}\right), \quad (39)$$

where $\Delta \eta^*$ is the adopted monotonic increase of the level of corrosion and λ_{i-1} is the previous final step

factor. In this case, there is no prescribed increase of load, displacement, displacement jump, etc.. Only the corrosion increases under constant load or displacement, i.e., at step time t, the step factor is given by the relative corrosion level:

$$\lambda(t) = \frac{\eta_t}{\eta_f}. \tag{40}$$

Note that, in this case, an incremental approach can not be adopted in a trivial manner. In fact, if no further increment of either displacement or force is enforced, the analysis can not proceed with the IA. In order to take into account the effect of the increase of corrosion, the structure must be reevaluated in each step, as done with the Total Iterative Approach. The bond–slip degradation leads to the increase of damage and to the decrease of the structure stiffness, which becomes apparent upon updating the internal variables and recalculating the structure again, under the previously defined loading.

4 Numerical tests

In this Section, numerical tests on reinforced concrete subjected to corrosion are presented, namely pullout tests and bending tests. In the pullout tests, special attention is given to local level analysis, namely to the transition modes between the bond–slip laws under increasing corrosion. In the bending tests, in which structural analysis is envisaged, the influence of: (i) the reduction of the resistant cross section of the steel bars (defined by r_{sane} in (26)), (ii) the stress normal to the concrete–steel interface and (iii) slippage of the reinforcement at the anchorage zone are also taken into account.

4.1 Pullout tests

The first pullout tests are obtained with the purpose of illustrating the transition modes between the bond–slip laws described in Sect. 2.2.

A steel bar ($A_s = 10$ mm^2) is modelled with truss elements, attached to the concrete by means of interface elements with initial zero thickness. The concrete specimen measures 160 mm (length) by 80 mm (height) by 10 mm (width). The Young's modulus of concrete is 32 GPa and the steel Young's modulus is 200 GPa. The concrete compressive strength is $f_c = 27.4$ MPa. The concrete specimen is fixed at the left edge. The

Table 1 Initial and final multilinear mode-II fracture relationships adopted for bond–slip

Initial bond–slip law ($\eta = 0$)		Final bond–slip law ($\eta_f = 0.2$)	
w_s (mm)	t_s (MPa)	w_s (mm)	t_s (MPa)
0.20	6.371	0.20	3.159
0.617	8.749	0.42	3.565
1.5	7.397	1.5	2.816
2.0	6.547	2.0	2.491
2.5	5.791	2.5	2.203
5.0	3.136	5.0	1.193
15.0	0.270	15.0	0.103
30.0	0.000	30.0	0.000

anchorage length is not considered so that the bar can slip at both edges of the concrete specimen.

It is assumed that the final level of corrosion, defined in (1), is $\eta_f = 0.2$ (20%), corresponding to the final bond–slip law given in Table 1. In Table 1, the initial bond–slip, corresponding to the pre-corrosion stage is also given. The initial law gives rise to a fracture energy $G_F^{II} = 47.2$, whereas a fracture energy $G_F^{II} = 18.2$ N/mm is obtained from the final law. In both cases, no confinement due to the stirrups is taken into account. The adopted bond–slip laws are taken from Silva (2018), Wu and Zhao (2013), Jiang et al. (2018). Note that the dimensions of both the concrete specimen and the steel bar are irrelevant with respect to the evaluated bond–slip relationship, only affecting the external force and corresponding displacement.

First, the horizontal displacement of the rightmost point of the bar is increased without corrosion, corresponding to function (36) in Sect. 3.2. Next, corrosion is introduced by means of the bond–slip degradation described in Sect. 2.2.3. The step size is still controlled by the displacement increment Δu_k^* (36), such that both the displacement and corrosion increase simultaneously. In Fig. 4, two bond–slip curves obtained at the right edge of the concrete specimen are shown. Each curve is obtained with a different initial bond stress level, before corrosion initiates. In both cases, the load is not allowed to increase (*fixed loading*, corresponding to cases 2. or 4. from Sect. 2.2). In the first case, a high bond stress value is first attained before corrosion ($t_s = 6.8$ MPa), lying above the ultimate cohesion ($|t_s| > c_f$), whereas in the second case a smaller bond value is reached ($t_s = 1.8$ MPa), which lies below the

ultimate cohesion ($|t_s| < c_f$). In the latter case, *snap-through* is allowed to a point at the softening branch of the final curve. In this way all tests can reach the final stage with zero bond stress. In this figure, the adopted finite element mesh is also represented as well as the initial and final bond–slip laws defined in Table 1.

In Fig. 5, the bond slip curves obtained along the bar from test (a) in Fig. 4 are presented. In this case all maximum bond stress values lie above the ultimate cohesion value.

In Fig. 6 two bond–slip curves are presented, corresponding to different corrosion rates. The solution is still displacement driven but the load is also allowed to increase, corresponding to case 1 in Sect. 2.2 (*variable loading*). It is clear that, in the test performed with the higher rate, the decrease of strength is anticipated with respect to the result obtained with the lower corrosion rate.

In the examples presented in Figs. 4, 5 and 6, both the Incremental Approach and the Total Iterative Approach can be used since the solution is displacement driven. As mentioned above, the solution is dependent on the corrosion rate which is defined here as a function of the displacement increment. The smaller the chosen ultimate displacement value $u_{k,final}$, the larger the corrosion rate $\Delta u_k^*/u_{k,final}$ (see Sect. 3.2). In the examples presented in Fig. 6, a value of $u_{k,final} = 30$ mm was adopted for the slower corrosion rate, whereas a value of $u_{k,final} = 5$ mm was adopted for the higher corrosion rate. Thus, in the latter case, for $u_k \geq 5$ mm the bond–slip curve lies on top of the final curve corresponding to $\eta_f = 0.2$, whereas in the former case, the final bond–slip law is only attained for $u_k = 30$ mm. Note that these input values ($u_{k,final} = 30$ mm; $u_{k,final} = 5$ mm) were chosen here to exemplify how to introduce rate dependence with this model.

The next examples are obtained with the Total Iterative Approach, with control function (39), defined in Sect. 3, in which the corrosion level is introduced explicitly as the step factor. In both cases, after reaching some loading stage, the corrosion is introduced and the structure is reevaluated at each step. In Fig. 7 the load is kept fixed whereas, in Fig. 8, the displacement obtained at the rightmost point of the bar, before corrosion is introduced, is kept fixed. In the former case (Fig. 7), the test stopped when the maximum bond stress lied above the peak bond stress of the current bond–slip law, which happened before the total corrosion level $\eta_f = 0.2$ was reached. In the second case (Fig. 8), the

test stopped when the total corrosion level was attained. This is why only 4 steps are obtained in the former case under corrosion, whereas 10 steps are needed in the second case. In both cases, each step corresponds to an increase of 10% of the corrosion level ($\Delta \eta^* = 0.02$ in (39)).

In Fig. 9, the bond slip curves obtained along the bar corresponding to Fig. 8 are presented. It is interesting to notice that, although the global displacement of the rightmost point of the bar is kept fixed, the slip displacement registered along the bar is not. This is due to the fact that, simultaneously to the slip increase, elastic unloading occurs in the steel bar. If the slip displacement was kept fixed, we would recover case 3 from Sect. 2.2.

4.2 Bending tests

In this Section bending tests are performed with the purpose of evaluating the influence, at structure level, of:

1. the degradation of the bond–slip law due to corrosion;
2. the reduction of the reinforcement bar effective cross section;
3. the dependence of the bond–slip law on the the stress normal to the interface and
4. the slippage of the reinforcement bar at the anchorage zone.

The finite element mesh and boundary conditions are presented on Fig. 10. The reinforcement bar is modelled using truss elements as done in Sect. 4.1. The beam is simply supported and is 2 m long, 20 cm high and 30 cm thick. The load is distributed on all top nodes of the beam. Concrete exhibits the same properties as in Sect. 4.1: Young modulus $E_c = 32$ GPa, compressive strength, $f_c = 27.4$ MPa., with compressive behaviour modelled as elastic-perfectly plastic. The concrete tensile strength is $f_t = 3$ MPa and bilinear softening is adopted under mode-I cracking, with a fracture energy $G_F = 0.1$ N/mm. The beam is reinforced with 3 bars of 16 mm ($3\phi16$) of steel S400 $f_{yk} = 400$ MPa, and Young modulus $E_s = 200$ GPa, modelled as elastic-perfectly plastic. The pre-corrosion and pos-corrosion bond–slip laws are given in Table 1. Several vertical prescribed cracks are defined across the length of the specimen in order to model multiple cracking due to

Fig. 4 Bond–slip curves obtained at the right edge of the specimen: *fixed loading* with corrosion introduced at high (**a**) and low (**b**) bond stress level
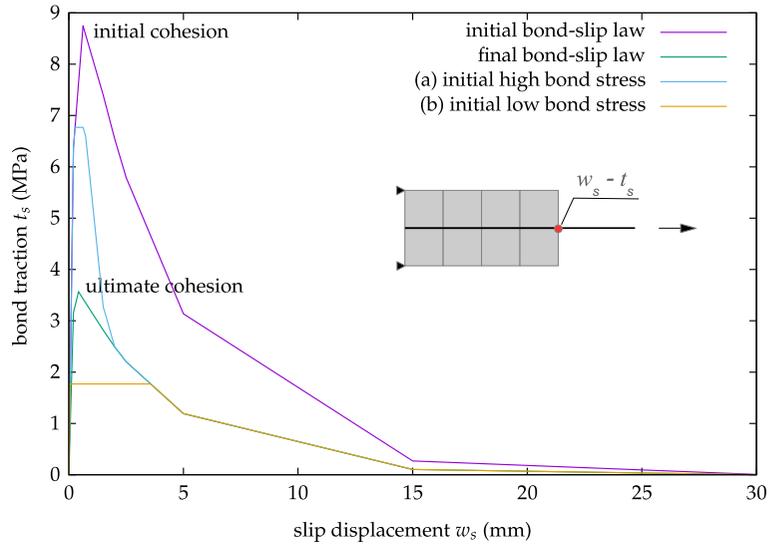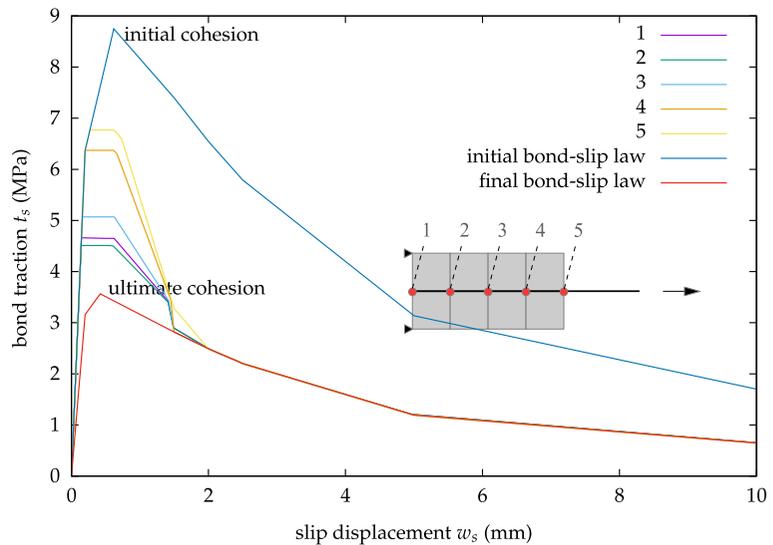

Fig. 5 Bond–slip curves obtained along the bar: *fixed loading*

tension-stiffening. The steel bar is located at 40 mm high, i.e., the cover corresponds to 32 mm. The connection between the left edge of the bar and the concrete is very stiff in order to simulate the effect of the anchorage length. Only half of the test is modelled due to symmetry.

In all subsequent examples, all the solutions obtained with corrosion are compared to the non-corroded numerical structural response, which is taken as reference.

4.2.1 Degradation of the bond–slip law due to corrosion

The first test is performed without corrosion, under proportional loading, designated hereafter as reference test. In order to evaluate the effect of tension-stiffening, the same test is also performed assuming perfect bond between concrete and steel. Both solutions are obtained under displacement control, i.e., using control function (36) from Sect. 3.2, with a small displacement increment at midspan, $\Delta u_k^* = -0.01$ mm ($\downarrow$). In Fig. 11, the deformed mesh obtained with bond–slip is shown.

Fig. 6 Bond–slip curves obtained at the right edge of the specimen: *variable loading* with low and high corrosion rates
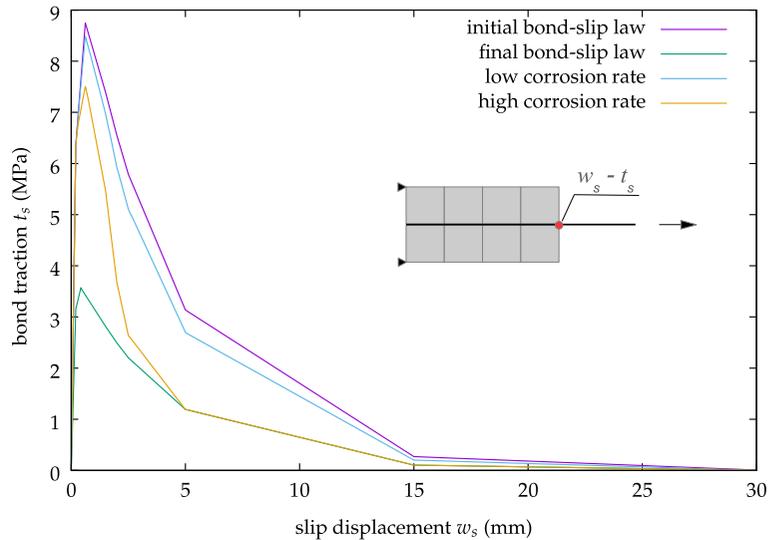
Fig. 7 Load–displacement curves obtained with increasing corrosion: fixed load
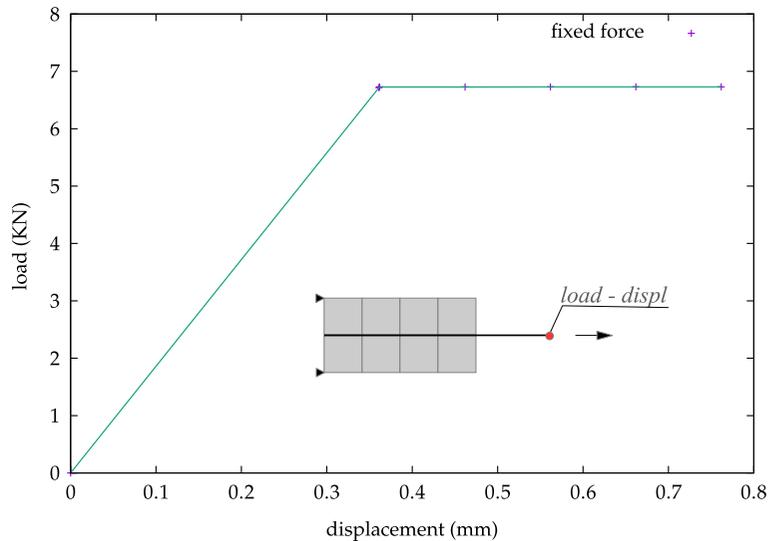
In Fig. 12, the load–displacement curves obtained with both tests are presented. In this figure, the displacement obtained at midspan is represented on the *x* axis, and the vertical nodal force applied at the symmetry line is represented on the *y* axis.

In this test, the tensile strength of concrete (3 MPa) is first reached at the central fictitious crack, at the symmetry line.[4] Next, fictitious cracks close to the central line also reach the tensile strength and start to dissipate energy. In the first steps, 4 fictitious cracks are evolving

simultaneously, the central crack and the three closest ones.

Each load drop in the reference load–displacement curve corresponds to crack localisation at some prescribed discontinuity due to tension-stiffening, which occurs simultaneously with unloading of the other fictitious cracks (Alfaiate and Sluys 2023).

Next, the test with corrosion is performed under nonproportional loading, with the following three loading stages:

1. the load is applied until a value of the force f_1 is reached, where f_1 is the pre-corrosion distributed load;

---

[4] Definition of fictitious crack is given in Hillerborg et al. (1976), and refers to the pre-crack stage, in which dissipation of energy occurs.

Fig. 8 Load–displacement curves obtained with increasing corrosion: fixed displacement
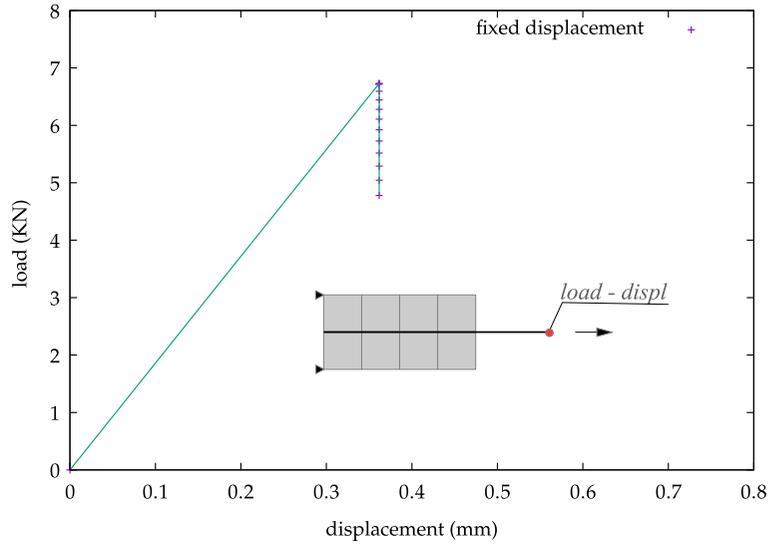
Fig. 9 Bond–slip curves obtained along the bar corresponding to Fig. 8
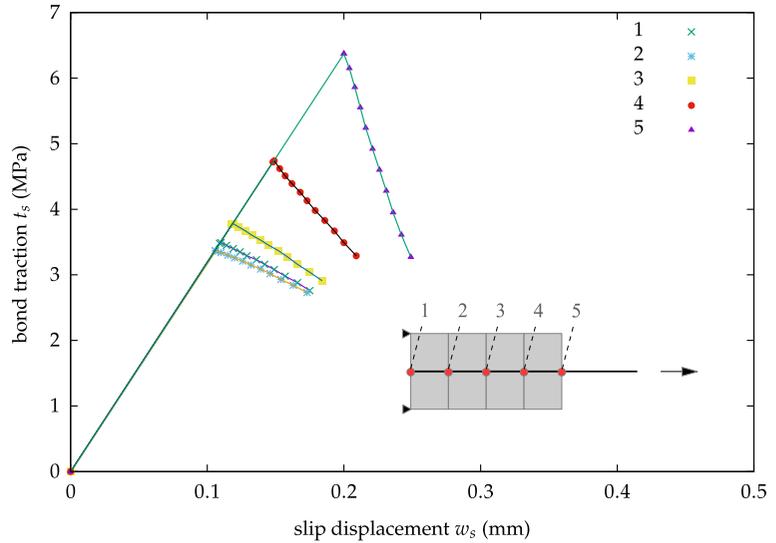
Fig. 10 Reinforced concrete beam: boundary conditions and adopted mesh
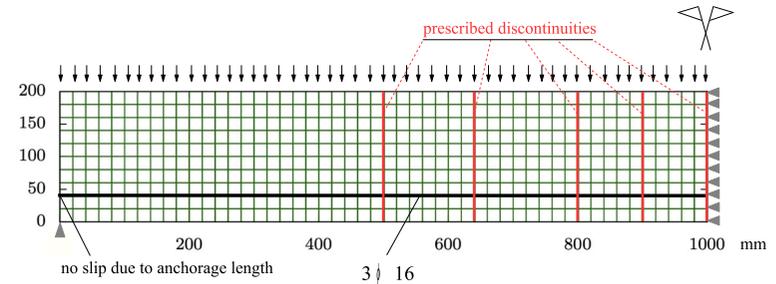
Fig. 11 Reinforced concrete test: deformed mesh (amplification displacement factor = 10)
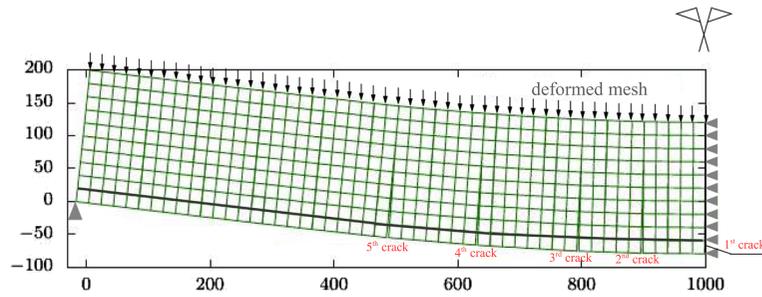
Fig. 12 Reinforced concrete tests: load–displacement curves obtained with displacement control, with and without bond–slip
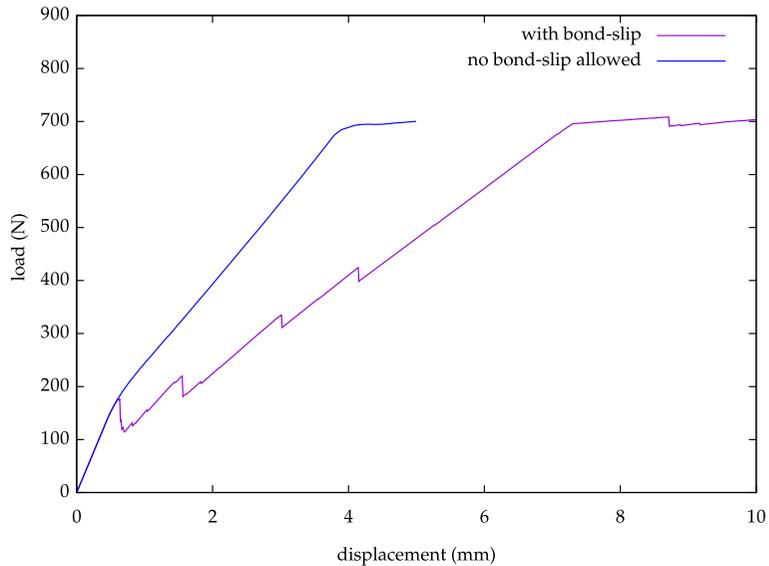
2. keeping the load f_1 fixed, corrosion is introduced according to control function given in (39) (*fixed loading*), adopting increments of $\Delta\eta^*$ in each step, until a value of the total corrosion level $\eta_f = 0.2$ is reached;
3. the load is increased again, under displacement control.

In the latter stage, the bond traction is allowed to increase, following the bond–slip relationship corresponding to the total corrosion level $\eta_f = 0.2$.

The corrosion is introduced at three different load levels f_1:

1. $f_1 = 15.6$ kN/m, corresponding to a vertical nodal force of $F_1 = 153$ N and displacement $u \approx 0.5$ mm at midspan;
2. $f_1 = 40.8$ kN/m, corresponding to a vertical nodal force of $F_1 = 400$ N and displacement $u \approx 4.0$ mm at midspan;

3. $f_1 = 67.4$ kN/m, corresponding to a vertical nodal force of $F_1 = 660$ N and displacement $u \approx 7.0$ mm at midspan;

In Fig. 13, the load–displacement curves obtained without and with corrosion corresponding to case 1 ($F_1 = 153$ N) are presented. During the corrosion stage no displacement increase at midspan is detected. However, the influence of corrosion is clear afterwards, in stage 3. Note that, although a noticeable reduction of the load is observed after the first peak due to the stiffness decrease, the obtained ultimate load is similar in both cases. The ultimate load lies on a plateau, in which the steel reinforcement reaches the plastic regime at midspan, i.e., $\sigma_{s|x=1.0\,\mathrm{m}} = f_y = 400$ MPa.

In Figs. 15 and 17, the load–displacement curves obtained with corrosion corresponding to cases 2. ($F_1 = 400$ N) and 3. ($F_1 = 660$ N), respectively, are plotted against the load–displacement curve obtained without corrosion.

Fig. 13 Load–displacement curves obtained without and with corrosion; case 1, corrosion introduced at $f_1 = 15.6$ kN/m, $F_1 = 153$ N
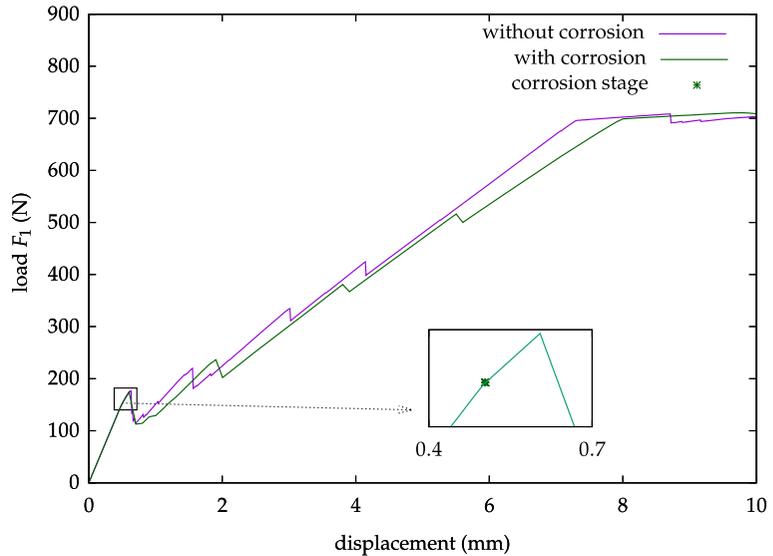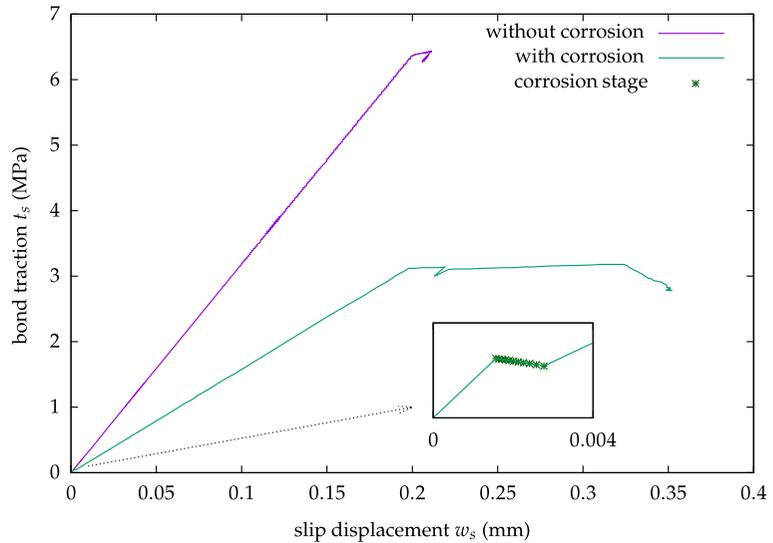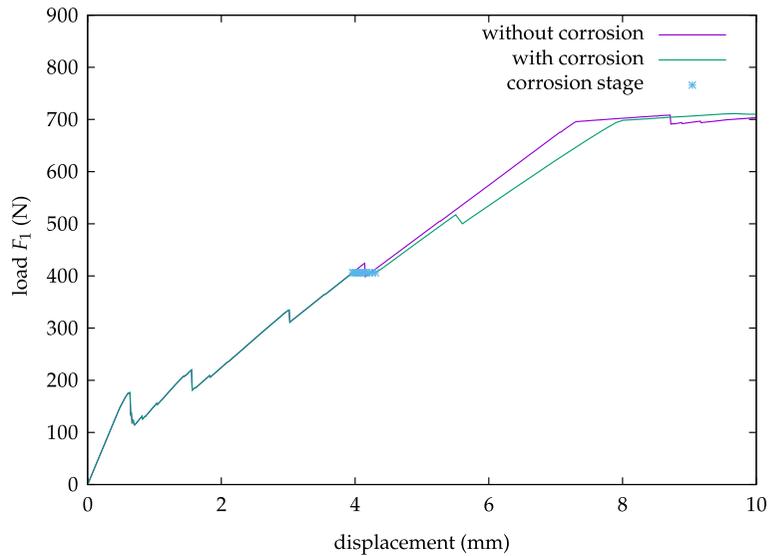

Fig. 14 Bond–slip curves obtained at $x = 500$ mm corresponding to case 1, Fig. 13

In Figs. 14, 16 and 18, the bond–slip curves corresponding to Figs. 13, 15 and 17, respectively, are presented, obtained at $x = 500$ mm, where maximum bond stress is achieved. In all these Figures, the corrosion stage is marked with a star(⋆). In Figs. 13 and 14, magnification of the curves near the corrosion stage is presented. It is interesting to see that, after stiffness decrease due to the introduction of corrosion, a plateau is reached in the bond–slip curve (Fig. 14), close to the maximum bond stress value of the final bond–slip relationship. In case 2 ($F_1 = 400$ N), bond stress decreases during stage 2 (Fig. 16), but some recovering is still possible under *variable loading*, before

the plateau is reached. In the last test ($F_1 = 660$ N), a pronounced decrease of the bond stress is obtained during stage 2 (Fig. 18). It is verified that, the higher the load level corresponding to the corrosion stage, the larger the displacement increase is obtained during stage 2. In all these tests the ultimate load obtained for the non-corroded specimen is similar to the ultimate load obtained from the tests with corrosion. As a consequence, the degradation of the bond–slip law alone does not give rise to a decrease of the strength of the beam.

Fig. 15 Load–displacement curves obtained without and with corrosion; case 2, corrosion introduced at $f_1 = 40.8$ kN/m, $F_1 = 400$ N
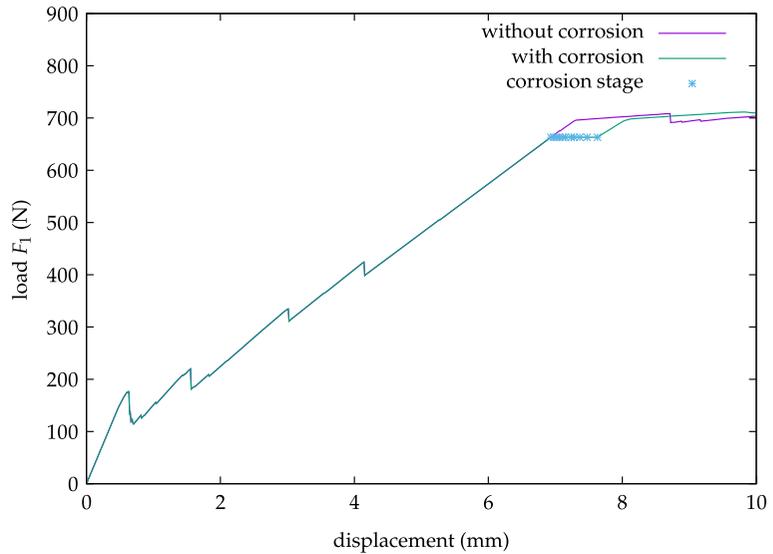

Fig. 16 Bond–slip curves obtained at $x = 500$ mm corresponding to case 2, Fig. 15
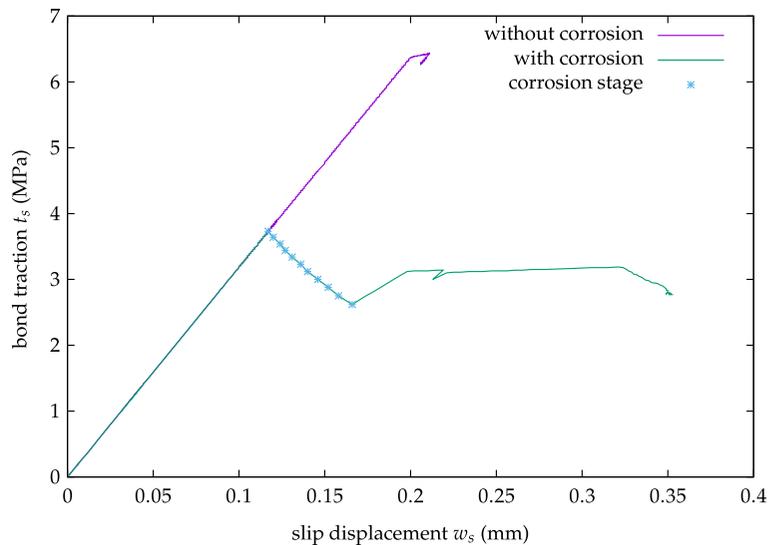
4.2.2 Reduction of the efective cross section of the reinforcement bar

According to Eq. (26), the reduction of the sane cross section of the bar (core reduction) is such that, at the end of the corrosion stage ($\eta_f = 0.2$), the radius of each bar decreases from 8 to $8 \times \sqrt{1 - 0.2} = 7.16$ mm, giving rise to a decrease of the total steel area of 20%, from 603.2 to 482.56 mm². In Fig. 19, the load–displacement curves obtained with no core reduction (from Fig. 13) and with core reduction are shown. The influence of the core reduction is clear, leading to a decrease of the structure stiffness. Furthermore, in this

test it is shown that premature failure can occur since the ultimate load decreases 83% with respect to the solution obtained without reduction of the cross section of the bars. In Fig. 20, the corresponding bond–slip curves are presented. It can be seen that the reduction of the sane cross section area of the bars gives rise to anticipation of softening in the bond–slip response.

In Fig. 21, the load–displacement curves corresponding to case 2 ($F_1 = 400$ N), obtained without core reduction (Fig. 15), and with core reduction are shown. A reduction in the ultimate load of 82% is found. In Fig. 22, the corresponding bond–slip curves are presented. The test corresponding to case 3 ($F_1 = 660$ N,

Fig. 17 Load–displacement curves obtained without and with corrosion; case 3, corrosion introduced at $f_1 = 67.4$ kN/m$F_1 = 660$ N

Fig. 18 Bond–slip curves obtained at $x = 500$ mm corresponding to case 3, Fig. 17
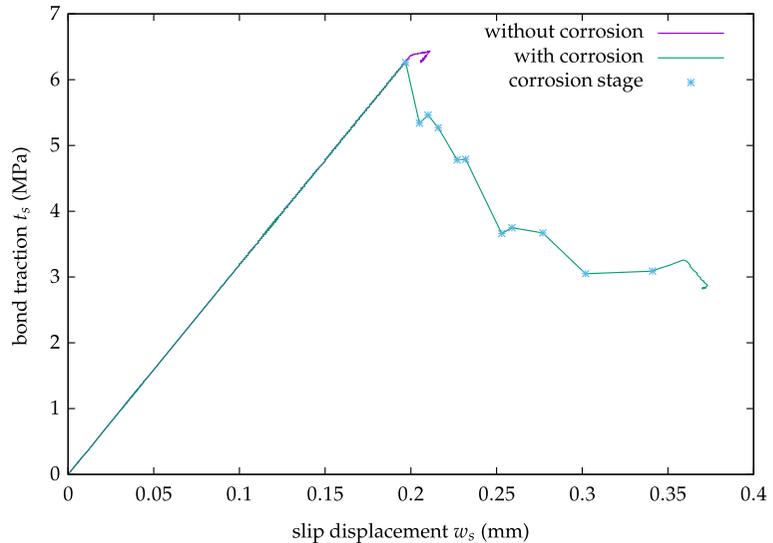

Fig. 17) fails upon introducing the first level of corrosion, $\eta = 0.02$, i.e., the strength decrease due to core reduction leads to an ultimate load below the applied force. As a consequence, under such a high level of loading, the beam can no longer withstand the force due to the decrease of the reinforcement area.

4.2.3 Dependence on the stress normal to the interface

In this Section, dependence of the bond–slip relationship on the stress state near the the concrete–steel interface is studied. In particular, the stress normal to

the concrete–steel interface is known to influence the bond–slip relationship, namely by affecting the cohesion. In this work, this influence is taken into account by means of the limit surface depicted in Fig. 2 and defined in (17) and (18). This effect can be considered in two ways:

1. taking into account the normal traction measured at the interface;
2. considering the stress value normal to the reinforcement bar obtained in the bulk, at the neighbourhood of the interface.

In all the examples presented in Sect. 4.2, the bar is modelled with truss elements and is *juxtaposed* to the

Fig. 19 Load–displacement curves obtained in case 1 (F_1 = 153 N), without and with core reduction
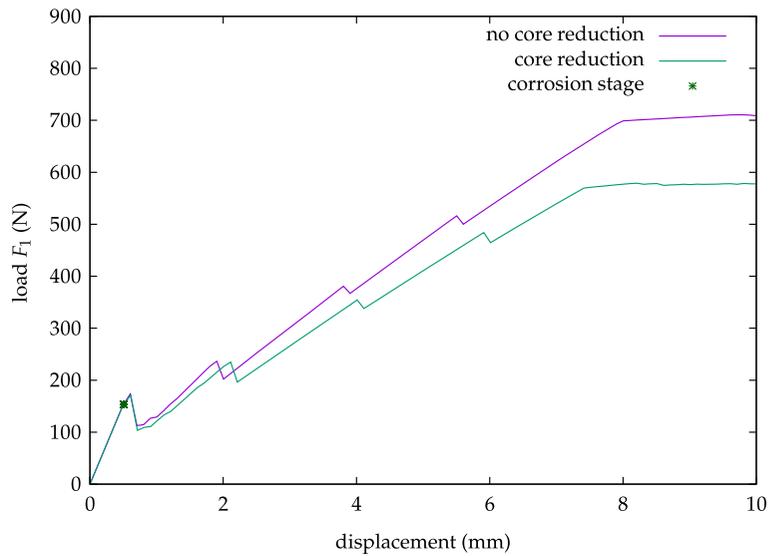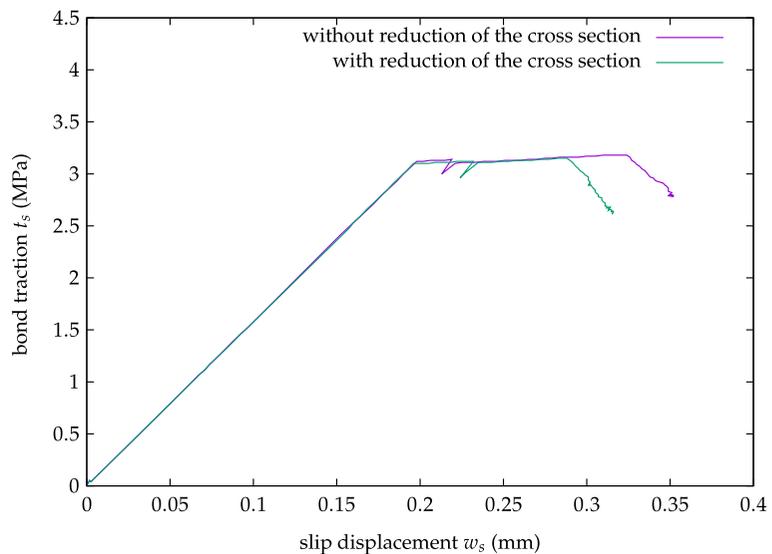

Fig. 20 Bond–slip curves obtained at $x = 500$ mm corresponding to case 1 (F_1 = 153 N), Fig. 19

beam, as depicted in Fig. 23. This is an adequate procedure to model the tangential bond–slip relation; nevertheless, the normal traction obtained at the interface does not provide a reliable measure of the action of the bulk material on the reinforcement bars. This is why option 2. is adopted here, in which the stress is taken as the average value obtained from bulk elements adjacent to the steel bar. Option 1 can be adopted in situations where more refined modelling of the reinforcement bar is used, with interfaces both above and below the bar, which is required to model spalling of the concrete cover.

The adopted bond–slip laws for corrosion used in the previous tests (Jiang et al. 2018; Silva 2018; Wu and Zhao 2013) are obtained from pullout tests, under pure shear ($\sigma_n = 0$). In order to take into account the dependence of the stress normal to the interface, the multilinear bond–slip curves adopted for corrosion in (29) are now modified according to:

$$t_s(m) = \left[t_{s0}(m) + \left(t_{sf}(m) - t_{s0}(m)\right) \times \frac{\eta_t}{\eta_f} \right] \times f_{surf},$$

(41)

where f_{surf} is a factor defined according to the limit surface (17)–(18), given by

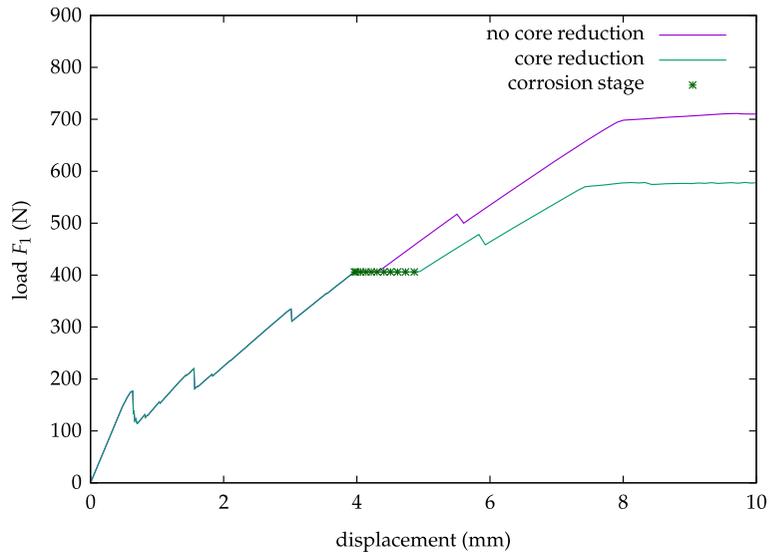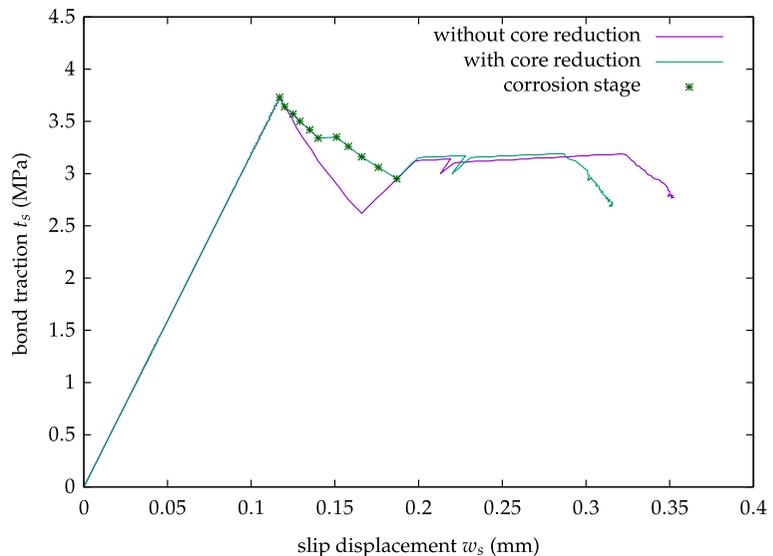**Fig. 21** Load–displacement curves obtained in case 2 ($F_1 = 400$ N), without and with core reduction

Fig. 22 Bond–slip curves obtained at $x = 500$ mm corresponding to case 2 ($F_1 = 400$ N)

$$f_{surf} = \frac{t_{s,surf}}{c}. \tag{42}$$

In (42), $t_{s,surf}$ is the bond traction lying on the limit surface, which depends on the stress normal to the interface and on the damage state, and c is the current cohesion value (10), which depends on the damage state (see Fig. 2). As a consequence, for $t_n = 0$, $t_{s,surf} = c$, for $t_n > 0$, $f_{surf} < 1.0$, whereas for $t_n < 0$, $f_{surf} > 1.0$.

The three loading stages defined in Sect. 4.2.1 are adopted. In Fig. 24, the load–displacement curve obtained with core reduction neglecting stress dependence is compared to the load–displacement curve obtained with core reduction taking into account stress dependence. In Fig. 25, the corresponding bond–slip curves are presented at $x = 500$ mm. In the latter figure is is clear that, although the bulk stress normal to the interface has a considerable influence on the bond–slip curve, by reducing the maximum bond stress, both load–displacement curves with core reduction remain similar, with the same ultimate load. In this example, the reduction of the bond stress was usually below 10%, with the exception of the cross section located at $x = 500$ mm, shown in Fig. 25, in which the reduction of the bond stress reached 18%, i.e., $f_{surf} \geq 0.82$, corresponding to a tensile stress value normal to the reinforcement bar, $\sigma_n = 1.4$ MPa. The maximum

Fig. 23 illustration of the use of truss element to model reinforcement bar
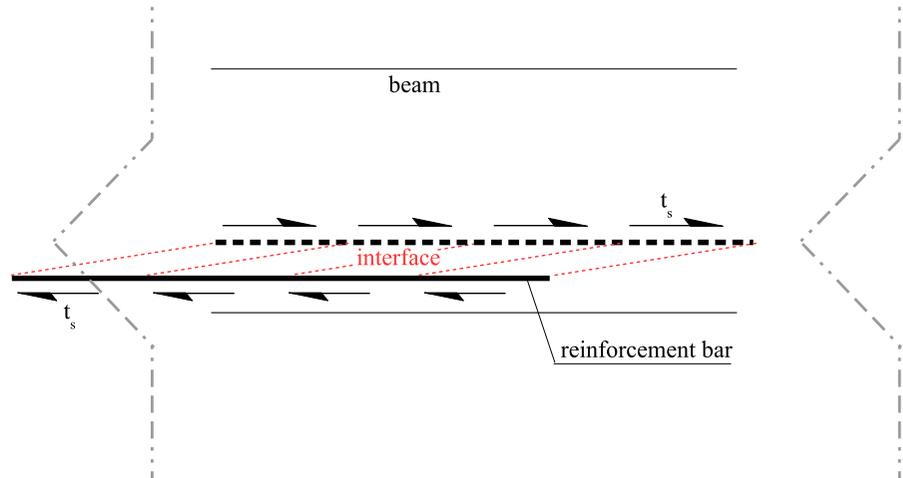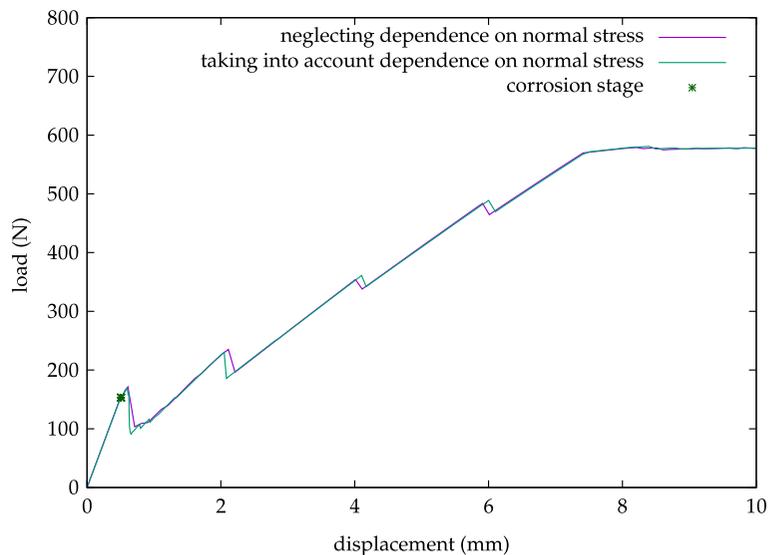

Fig. 24 Load–displacement curves neglecting stress dependence and taking into account stress dependence—case 1 ($F_1 = 153$ N)

compressive stress in the neighbourhood of the bar was obtained at $x = 40$ mm, $\sigma_n = -0.73$ MPa, giving rise to an increase of the bond stress given by $f_{surf} = 1.06$.

In Figs. 26 and 27, the corresponding results obtained with case 2 ($F_1 = 400$ N) are presented. Similar conclusions can be drawn in both cases 1 and 2.

In Figs. 28, 29 and 30, the distributions along the length of the bar of (i) the bulk stress normal to the concrete–steel interface σ_n, and (ii) the bond traction t_s, for case 1 ($F_1 = 153$ N), are presented. In Fig. 28, the distributions of σ_n and t_s obtained at the end of the corrosion stage (stage 2) are presented. In Fig. 29 the distributions of σ_n and t_s obtained under the maximum normal stress value attained in loading stage 3 are presented ($\sigma_{n,max} = 1.4$ MPa, registered at $x = 500$ mm).

In Fig. 30 the distributions of σ_n and t_s obtained under the minimum normal stress value attained in loading stage 3 are presented ($\sigma_{n,min} = -0.73$ MPa, registered at $x = 40$ mm).

It is interesting to see that, in the former case (Fig. 28), localisation had occurred at the second crack only, where a change in sign in the bond traction is captured, whereas in the other cases (Figs. 29, 30) localisation had occurred at all discontinuities.

4.2.4 Slippage of the anchorage zone

In the previous tests, although degradation of the bond–slip relationship occurs due to corrosion and is also affected by the stress normal to the interface, slip

Fig. 25 Bond–slip curves obtained at $x = 500$ mm corresponding to case 1 ($F_1 = 153$ N)
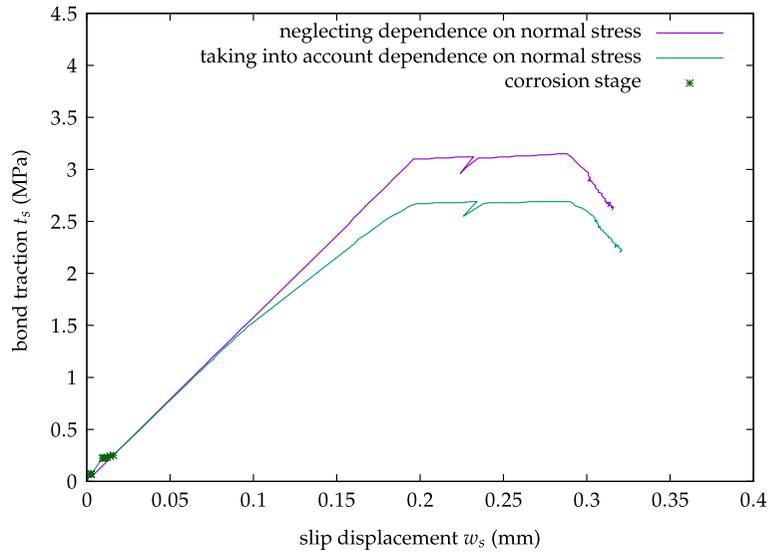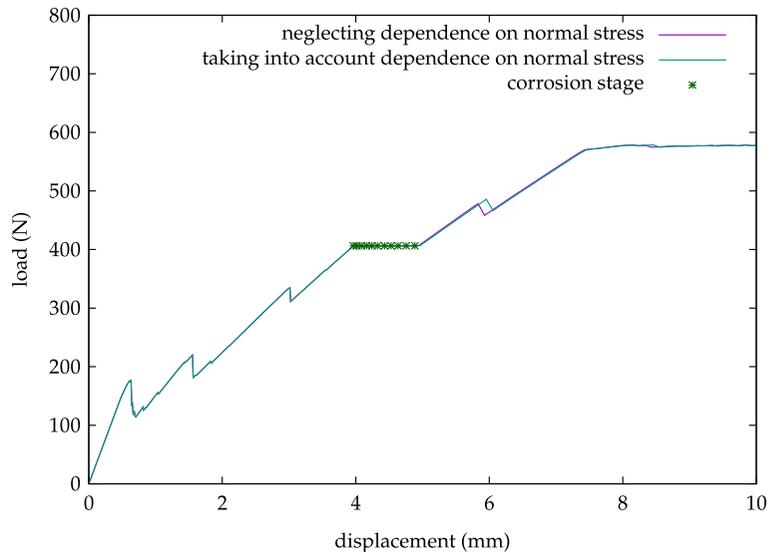

Fig. 26 Load–displacement curves neglecting stress dependence and taking into account stress dependence - case 2 ($F_1 = 400$ N)

between concrete and steel is not allowed to occur at two locations: (i) the left edge of the beam, to simulate the anchorage length and (ii) at midspan, due to symmetry. As a consequence, the obtained ultimate load is practically the same with and without corrosion as long as the area of steel bars remains unchanged.

This is in agreement with the results shown in Figs. 13, 15 and 17. The same conclusion can be withdrawn from Figs. 24 and 26, i.e., the same area of the cross section of the reinforcement bars leads to the same ultimate load, independently from the other factors.

Even if the steel bar is allowed to slip at the anchorage zone, the bond strength is distributed along the whole length of the interface and may still withstand the full load. In Fig. 31, the load–displacement curves obtained with and without slippage of the anchorage zone are presented, keeping the corrosion level adopted in the previous examples ($\eta_f = 0.2$). In these examples no reduction of the cross section is adopted. It is observed that, allowing slippage at the anchorage zones does not lead to a decrease of the ultimate load.

In fact, only by enforcing a greater degree of corrosion this effect can give rise to premature failure of the beam. In order to allow for this possibility, the residual bond–slip law defined in Table 2 is adopted ($G_F^{II} = 4.47$ N/mm) (Silva 2018), corresponding to

Fig. 27 Bond–slip curves obtained at $x = 500$ mm corresponding to case 2 ($F_1 = 400$ N)
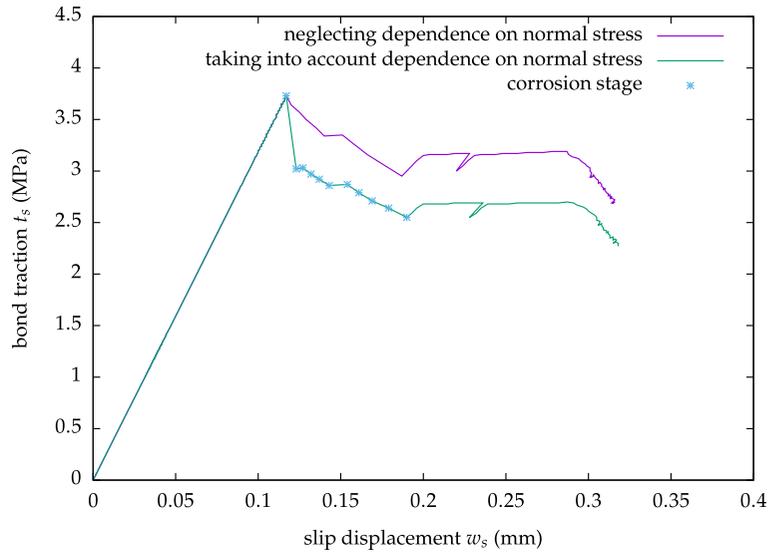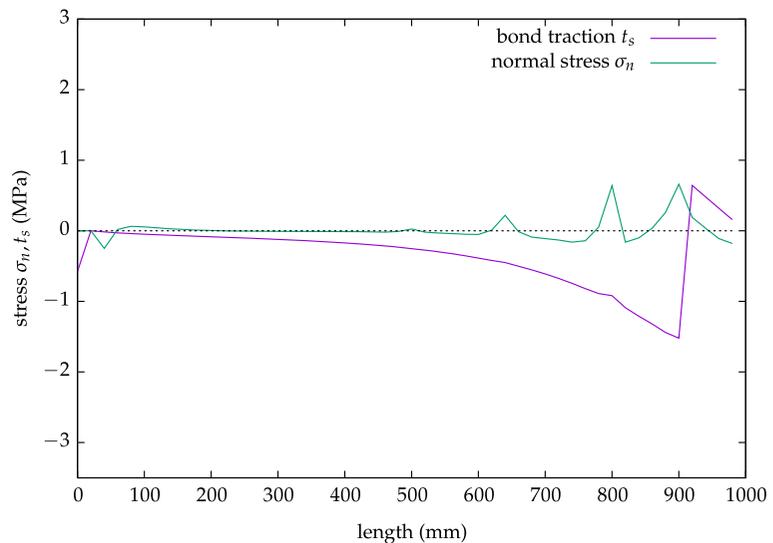

Fig. 28 Bond traction and normal stress along the length of the bar, obtained at the end of the corrosion stage (loading stage 2)

a higher degree of corrosion. In Fig. 32, the respective load–displacement curve is compared to the load–displacement curve obtained without slippage of the anchorage zone. It can be observed that, due to the increase of corrosion, a considerable drop of the ultimate load occurs due to slippage of the reinforcement bars (18%).

5 Final remarks

In this work, numerical analyses of steel corrosion in reinforced concrete are performed. Special attention is given to macro-mechanical aspects which influence the structural behaviour, namely:

1. the degradation of concrete–steel bond–slip relationship;
2. the reduction of the sane cross section of the reinforcement bar;
3. the influence of the stress normal to the reinforcement bar at the neighbourhood of the concrete–steel interface;
4. the rate of corrosion;
5. slippage of the reinforcement at the anchorage zone.

A Total Iterative Approach is adopted such that the structure is reevaluated in each step under progressive damage evolution, using the secant matrix.

Fig. 29 Bond traction and normal stress along the length of the bar, under maximum normal stress obtained in loading stage 3
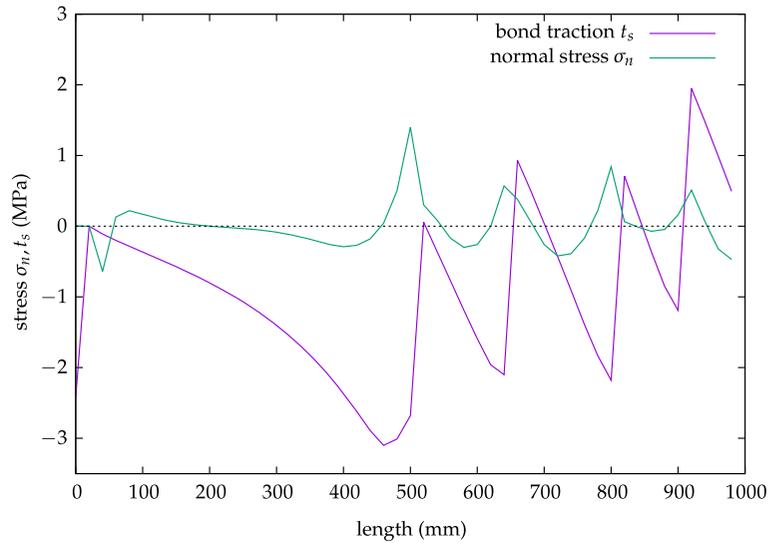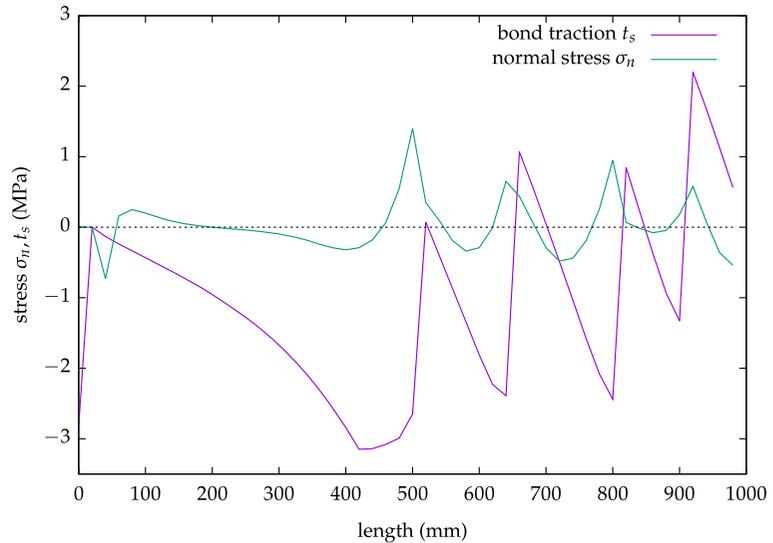

Fig. 30 Bond traction and normal stress along the length of the bar, under minimum normal stress obtained in loading stage 3

Corrosion gives rise to the degradation of the bond behaviour, which is modelled with the introduction of transition modes between evolving bond–slip laws. Several numerical pullout tests were first performed, to illustrate the implementation of the model at local level. Next, bending tests were performed to evaluate the structural behaviour of a reinforced concrete beam submitted to corrosion. The main conclusions from the bending tests are:

1. the higher the load level corresponding to the initiation of the corrosion stage, the larger the corresponding increase in displacement;

2. degradation of the bond–slip law due to corrosion affects mainly the stiffness of the structure, giving rise to displacement increase;

3. degradation of the bond–slip law alone does not lead to a decrease of the ultimate load;

4. the degradation of the bond–slip law leads to premature softening of the bond–slip relationship, although not to the decrease of maximum bond traction;

5. the reduction of the uncorroded cross section of the reinforcement bars gives rise to the decrease of the ultimate load and premature failure of the structure;

Fig. 31 Load–displacement curves obtained without and with slippage of the anchorage zone under residual bond–slip law given in Table 1—case 1 ($F_1 =$ 153 N), no core reduction
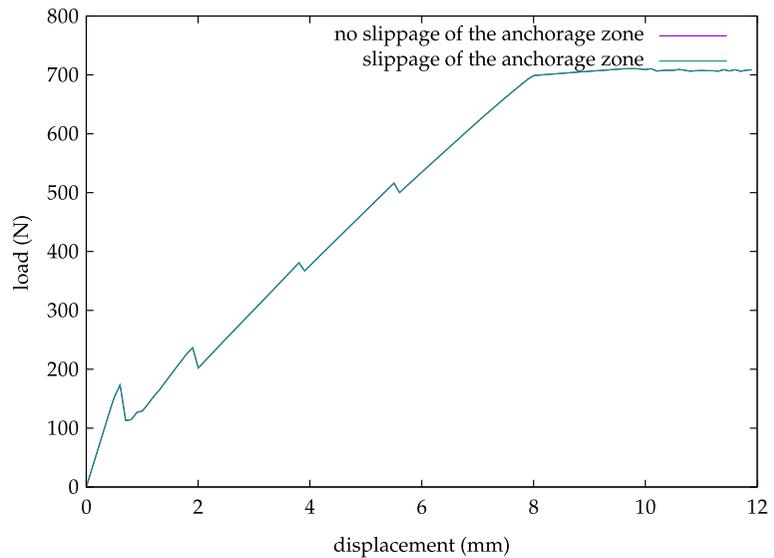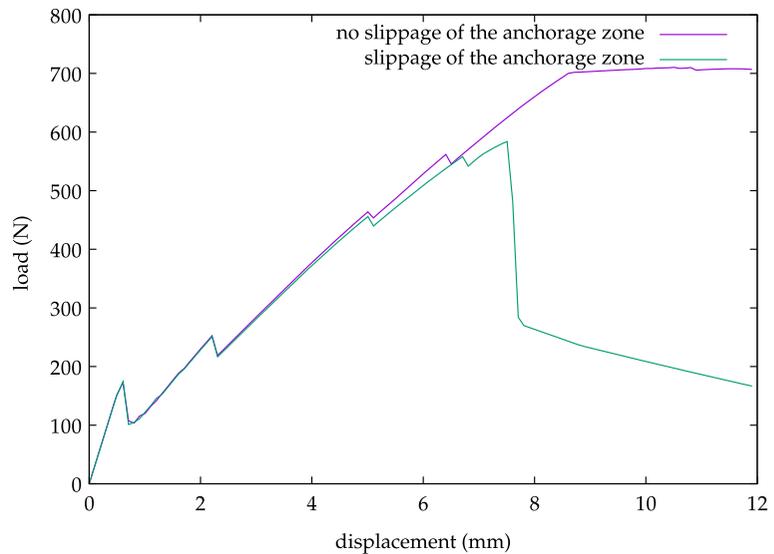

Fig. 32 Load–displacement curves obtained without and with slippage of the anchorage zone under residual bond–slip law given in Table 2—case 1 ($F_1 =$ 153 N), no core reduction

6. the influence of the tensile stress normal to the concrete–steel interface leads to the decrease in the stiffness of the bond–slip law and to the reduction of the maximum bond traction;

7. under severe corrosion conditions, slippage of the reinforcement at the anchorage zone may lead to a decrease of the ultimate load and premature failure of the structure.

Finally, it is shown that both the mechanical and the numerical approaches adopted are adequate to model corrosion in reinforced concrete structures.

Table 2 Initial and final multilinear mode-II fracture relationships adopted for bond–slip in Fig. 32

Initial bond–slip law		Final bond–slip law	
w_s (mm)	t_s (MPa)	w_s (mm)	t_s (MPa)
0.20	6.371	0.20	2.159
0.617	8.749	0.42	1.565
1.5	7.397	1.5	0.816
2.0	6.547	5.0	0.200
2.5	5.791	15.0	0.000
5.0	3.136		
15.0	0.270		
30.0	0.000		

Declarations

References

Alfaiate J, Sluys LJ (2017a) On the modelling of mixed-mode fracture: Part I—localised damage models. Eng Fract Mech 182:157–186

Alfaiate J, Sluys LJ (2017b) On the modelling of mixed-mode fracture: Part II—inclusion of dilatancy. Eng Fract Mech 182:245–264

Alfaiate J, Sluys LJ (2018) On the use of non-iterative methods in cohesive fracture. Int J Fract 210:167–186

Alfaiate J, Sluys LJ (2019) Damage and fracture mechanics approaches to mixed-mode discrete fracture with dilatancy. Theoret Appl Fract Mech 104:102350. https://doi.org/10.1016/j.tafmec.2019.102350

Alfaiate J, Sluys LJ (2023) A novel, total-iterative approach to model quasi-brittle materials. Eng Fract Mech 277:108955. https://doi.org/10.1016/j.engfracmech.2022.108955

Andrade C, Molina F, Alonso C (1993) Cover cracking as a function of rebar corrosion: Part 1. Experimental test. Mater Struct 26:453–464

Apostolopoulos CA, Koulouris KF, Apostolopoulos AC (2022) Correlation of surface cracks of concrete due to corrosion and bond strength (between steel bar and concrete). Hindawi Adv Civil Eng. https://doi.org/10.1155/2019/3438743

Bastos R (2022) Bond model of steel reinforcement embedded in low binder concrete. Master's thesis, Instituto Superior Técnico, Universidade de Lisboa, Portugal

Chenjie Y (2019) From sequentially linear analysis to incremental sequentially linear analysis. robust algorithms for solving the non-linear equations of structures of quasi-brittle materials. PhD thesis, TUDelft, The Netherlands

Chernin L, Val DV (2011) Prediction of corrosion-induced cover cracking in reinforced concrete structures. Constr Build Mater 25(4):1854–1869

Coronelli D (1998) Bar corrosion in steel-concrete bond: material and structural effects in r/c. PhD thesis, Politecnico di Milano, Italy

Costa R, Alfaiate J (2006) The numerical analysis of reinforced concrete beams using embedded discontinuities. Struct Durab Health Monit 2(1):11–18

Costa R, Alfaiate J, Dias-da-Costa D, Sluys LJ (2012) A non-iterative approach for the modeling of quasi-brittle materials. Int J Fract 178(1–2):281–298

Costa R, Alfaiate J, Dias-da-Costa D, Neto P, Sluys LJ (2013) Generalisation of non-iterative methods for the modelling of structures under non-proportional loading. Int J Fract 21–2:21–38

DeJong MJ, Hendriks MAN, Rots JG (2008) Sequentially linear analysis of fracture under non-proportional loading. Eng Fract Mech 75(18):5042–5056

Fang C, Lundgren K, Chen L, Zhu C (2004) Corrosion influence on bond in reinforced concrete. Cem Concr Res 34:2159–2167

Gago AS, Alfaiate J, Lamas A (2011) The effect of the infill in arched structures: analytical and numerical modelling. Eng Struct 33(5):1450–1458

Guzmán S, Gálvez JC (2017) Modelling of concrete cover cracking due to non-uniform corrosion of reinforcing steel. Constr Build Mater 155:1063–1071

Guzmán S, Gálvez JC, Sancho JM (2011) Cover cracking of reinforced concrete due to rebar corrosion induced by chloride penetration. Cem Concr Res 41:893–902

Guzmán S, Gálvez JC, Sancho JM (2014) Modelling of chloride ingress into concrete through a single-ion approach. application to an idealized surface crack pattern. Int J Numer Anal Methods Geomech 38:1683–1706

Hillerborg A, Modeer M, Petersson PE (1976) Analysis of crack formation and crack growth in concrete by means of fracture mechanics and finite elements. Cem Concr Res 6(6):773–782

Jiang C, Wu YF, Dai MJ (2018) Degradation of steel-to-concrete bond due to corrosion. Constr Build Mater 158:1073–1080

Koulouris K, Apostolopoulos C (2021) Study of the residual bond strength between corroded steel bars and concrete—a com-

parison with the recommendations of fib model code 2010. Metals 11:757. https://doi.org/10.3390/met11050757

Lilliu G, van Mier JGM (2003) 3d lattice type fracture model for concrete. Eng Fract Mech 70(7–8):927–941

Lin H, Zhao Y (2016) Effects of confinements on the bond strength between concrete and corroded steel bars. Constr Build Mater 118:127–138. https://doi.org/10.1016/j.conbuildmat.2016.05.040

Louro AS (2014) Characterization of bond of ribbed bars subjected to repeated and alternating actions. PhD thesis, Universidade Nova de Lisboa

Lundgren K (2005) Bond between ribbed bars and concrete: Part 2. The effect of corrosion. Mag Concr Res 57(7):383–396

Mak MWT, Lees JM (2022) Bond strength and confinement in reinforced concrete. Constr Build Mater 355:129012. https://doi.org/10.1016/j.conbuildmat.2022.129012

Mak MWT, Desnerck P, Lees JM (2019) Corrosion-induced cracking and bond strength in reinforced concrete. Constr Build Mater 208:228–241. https://doi.org/10.1016/j.conbuildmat.2019.02.151

Molina F, Alonso C, Andrade C (1993) Cover cracking as a function of rebar corrosion: Part 2. Numerical model. Mater Struct 26:532–548

Ožbolt J, Oršanić F, Balabanić G (2017) Modelling processes related to corrosion of reinforcement in concrete: coupled 3d finite element model. Struct Infrasctrut Eng 13:135–146

Rots JG (2001) Sequentially linear continuum model for concrete fracture. In: de Borst R, Mazars J, Pijaudier-Cabot G, van Mier JGM (eds) Fracture mechanics of concrete structures—FRAMCOS4. France, Paris, pp 831–840

Rots JG, Invernizzi S (2003) Regularized sequentially linear saw-tooth softening model. Int J Numer Anal Methods Geomech 28:821–856

Rots JG, Belletti B, Invernizzi S (2008) Robust modeling of rc structures with an "event- by-event" strategy. Eng Fract Mech 75(3–4):590–614

Sanz B, Planas J, Sancho JM (2016) Study of the influence of the oxide and concrete parameters on the results of accelerated corrosion tests. Procedia Struct Integrity 2:2849–2856

Schlangen E, van Mier JGM (1992) Experimental and numerical analysis of micromechanisms of fracture of cement-based composites. Cement Concr Compos 14(12):105–118

Silva J (2018) Análise do comportamento de vigas de betão armado com dano induzido por deterioração. Master's thesis, Instituto Superior Técnico, Universidade de Lisboa, Portugal

Slobbe AT, Hendriks MAN, Rots JG (2012) Sequentially linear analysis of shear critical reinforced concrete beams without shear reinforcement. Finite Elem Anal Des 50:108–124

Tahershamsi M, Fernandez I, Lundgren K, Zandi K (2016) Investigating correlations between crack width, corrosion level and anchorage capacity. Struct Infrastruct Eng 13(10):1294–1307. https://doi.org/10.1080/15732479.2016.1263673

Wu Y, Zhao X (2013) Unified bond stress-slip model for reinforced concrete. ASCE J Struct Eng 139(11):1951–1962. https://doi.org/10.1061/(ASCE)ST.1943-541X.0000747

Zhou HJ, Liang XB, Zhang XL, Lu JL, Xing F, Mei L (2017) Variation and degradation of steel and concrete bond performance with corroded stirrups. Constr Build Mater 138:56–68. https://doi.org/10.1016/j.conbuildmat.2017.02.007

Publisher's Note Springer Nature remains neutral with regard to jurisdictional claims in published maps and institutional affiliations.